

Slow dynamics and magnon bound states in the 2D long-range quantum Ising model

Vighnesh Dattatraya Naik¹ and Markus Heyl^{1,2}

¹*Theoretical Physics III, Center for Electronic Correlations and Magnetism, Institute of Physics, University of Augsburg, 86135 Augsburg, Germany*

²*Centre for Advanced Analytics and Predictive Sciences (CAAPS), University of Augsburg, Universitätsstr. 12a, 86159 Augsburg, Germany*

(Dated: December 11, 2025)

The dynamics of long-range quantum Ising models represents a current frontier in experimental physics, notably in trapped ions or Rydberg atomic systems. However, a theoretical description of these dynamics beyond 1D remains a significant challenge for conventional methods. Here, we address this challenge by means of neural quantum states to simulate global quenches from the fully polarized ferromagnetic state in the 2D quantum Ising model with power-law decaying interactions. From these numerically exact simulations, we find that the dynamics exhibit slow relaxation with long-lived oscillations. We explain this behavior through a theory for the formation of magnon bound states, which are generated, as we show, through effective attractive interactions between magnons that persist over several lattice sites due to the power-law nature of the interactions. Our results are readily observable in current quantum simulation platforms realizing long-range interacting models such as in Rydberg atomic systems.

Introduction.—Long-range interacting quantum systems arise across atomic, molecular, optical, and solid-state platforms [1], with prototypical realizations provided by spin models with power-law couplings in trapped ions [2–8], Rydberg atom arrays [9–11], and dipolar quantum gases [12–16]. Their tunable interaction range provides a controlled setting to investigate how nonlocal couplings reshape quantum dynamics.

In one dimension, theoretical and experimental studies have established that long-range interactions modify correlation spreading and the effective light-cone structure [3, 17], affect entanglement growth [4], and generate prethermal plateaus and long-lived oscillations that delay thermalization [18]. These phenomena have been linked to emergent quasiparticles, such as domain walls or magnons, their mutual interactions, and the bound states they form [4, 8, 19–23]. However, extending these insights to two dimensions remains a central open problem. The exponential growth of the Hilbert space together with the rapid buildup of entanglement makes well-established methods such as exact diagonalization and standard tensor-network methods (e.g., tDMRG/MPS) challenging. Consequently, the quantum dynamics of 2D long-range models remain largely unexplored. The interplay between 2D geometry and power-law interactions raises new questions about the nature of the elementary excitations: Can nonlocal interactions in 2D bind distant excitations? How do they impact thermalization?

In this work, we address these challenges by combining large-scale numerical simulations with an effective theoretical description. We employ neural quantum states (NQS) [24–27] to simulate the real-time dynamics of the 2D long-range transverse-field Ising model following global quenches, accessing unprecedentedly large time scales and system sizes. Starting from the fully polarized ferromagnetic state, we observe a slow buildup of

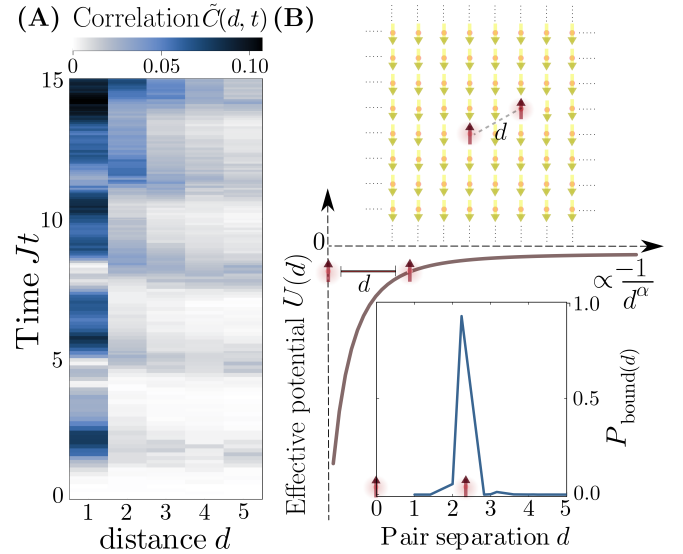


FIG. 1. Slow dynamics and magnon binding. (A) Spatiotemporal normalized connected correlator $\tilde{C}(d, t)$ after a quench from $|\downarrow \cdots \downarrow\rangle$ on an 11×11 lattice ($\alpha = 3$, $g/J = 0.2$), showing slow dynamics and oscillations. (B) Schematic illustration of two magnons at separation d . The lower panel sketches the effective attractive potential $U(d)$ for $\alpha = 3$ from Eq. 4. Inset: the corresponding two-magnon bound-state probability peaked at $\tilde{r} = \sqrt{5}$ on an 101×101 lattice.

correlations accompanied by persistent oscillations. To interpret this behavior, we construct an effective few-body theory whose eigenspectrum shows excellent agreement with the Fourier spectral analysis of the time evolution. Crucially, the effective model reveals that the long-range interactions mediate a power-law attraction between magnons, yielding multi-magnon bound states even at separations of several lattice sites, leading to a large number of bound states. Thus, we identify these

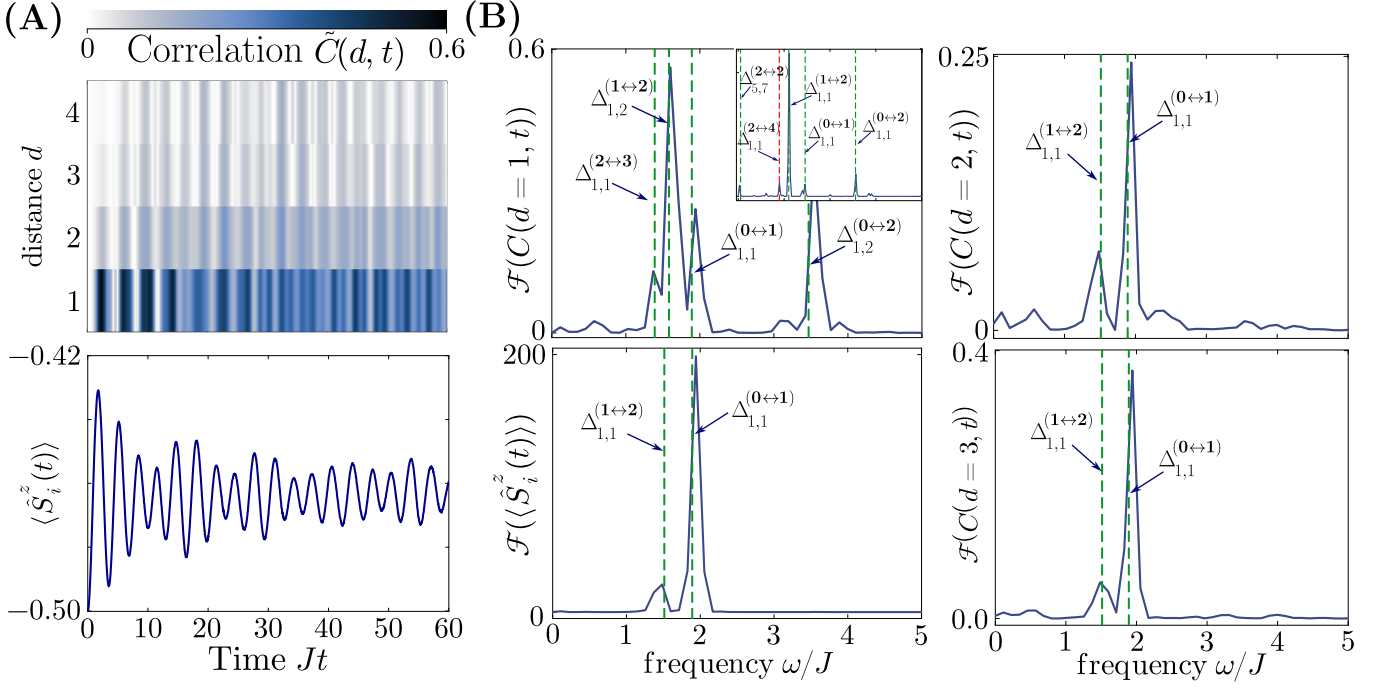


FIG. 2. Fourier spectroscopy for the post-quench dynamics (9×9 , $\alpha = 3$ and $g/J = 0.5$). (A) Spatiotemporal connected correlator $\tilde{C}(d, t)$, together with the site-averaged longitudinal magnetization $\langle \hat{S}_i^z(t) \rangle$. (B) FFTs $\mathcal{F}[C(d, t)]$ for $d = 1, 2, 3$, and $\mathcal{F}[\langle \hat{S}_i^z(t) \rangle]$, plotted versus frequency ω/J . Vertical dashed lines mark energy gaps $\Delta_{i,j}^{\nu \leftrightarrow \nu'} = E_i^\nu - E_j^{\nu'}$ from effective Hamiltonians restricted to the ν magnon sectors. The matching between spectral peaks and energy gaps quantitatively validates the few-body effective description. Inset: Fourier spectra of exact dynamics for a 5×5 system (evolved up to $Jt = 200$).

bound states as the relevant quasiparticles for the slow relaxation. These findings provide an experimentally accessible framework for exploring non-equilibrium dynamics in 2D long-range quantum matter.

Model.— We consider the 2D long-range quantum Ising model described by the Hamiltonian

$$\hat{H} = -\frac{J}{\mathcal{N}_\alpha} \sum_{i \neq j} \frac{\hat{S}_i^z \hat{S}_j^z}{r_{ij}^\alpha} - g \sum_i \hat{S}_i^x, \quad (1)$$

where \hat{S}_i^μ ($\mu = x, y, z$) are spin-1/2 operators on a square lattice of size $L \times L$ with periodic boundary conditions, and r_{ij} denotes the distance between sites i and j . The exponent α controls the range of the interaction: small values of α correspond to slowly decaying couplings, while $\alpha \rightarrow \infty$ recovers the nearest-neighbor limit. We employ Kac normalization $\mathcal{N}_\alpha = (L^2 - 1)^{-1} \sum_{i < j} r_{ij}^{-\alpha}$, which keeps the energy per site finite as $L \rightarrow \infty$.

Quench protocol and NQS simulations.— We study the real-time dynamics following a global quench from the fully polarized initial state $|\psi_0\rangle = \bigotimes_i |\downarrow_i\rangle$ to a finite g . Motivated by the broad experimental availability of dipolar interactions, we consider the dipolar case with exponent $\alpha = 3$ as a representative of long-range interactions. Time evolution is governed by $|\psi(t)\rangle = e^{-i\hat{H}t} |\psi_0\rangle$, and we monitor the longitudinal magnetization $\langle \hat{S}_i^z(t) \rangle$ and

the spin-spin correlation function

$$C(d, t) = \langle \hat{S}_i^z(t) \hat{S}_{i+d}^z(t) \rangle - \langle \hat{S}_i^z(t) \rangle \langle \hat{S}_{i+d}^z(t) \rangle, \quad (2)$$

measured along the x-direction of the lattice. To compare dynamics across different α and g , we plot the normalized correlator $\tilde{C}(d, t) = C(d, t) \cdot \frac{8\mathcal{N}_\alpha J^2}{g^2}$, which removes the parameter-dependent amplitude scaling.

To reach system sizes beyond the limits of exact diagonalization for real-time simulations, we employ neural quantum states (NQS), a variational representation of quantum wavefunctions using artificial neural networks. Within NQS, the time-dependent state $|\psi_{\theta(t)}\rangle = \sum_S \psi_{\theta(t)}(S) |S\rangle$, with $|S\rangle$ denoting the full set of 2^N spin configurations, is represented through wave-function amplitudes $\psi_{\theta(t)}(S)$ which are parametrized by network weights θ . The evolution of these parameters, $\theta(t)$, is governed by the time-dependent variational principle. Importantly, NQS provides a numerically exact solution of the dynamics in the sense that convergence is guaranteed upon increasing the size of the underlying artificial neural network. Specifically, we use a convolutional neural network (CNN) architecture based on the ResNet framework Ref. [28–30], which is optimized for translational invariance and to capture 2D spatial correlations.

Our numerical results, obtained via NQS simulations, show that for an 11×11 lattice [Fig. 1(A)], the spatiotemporal correlations $\tilde{C}(d, t)$ build up only slowly, ex-

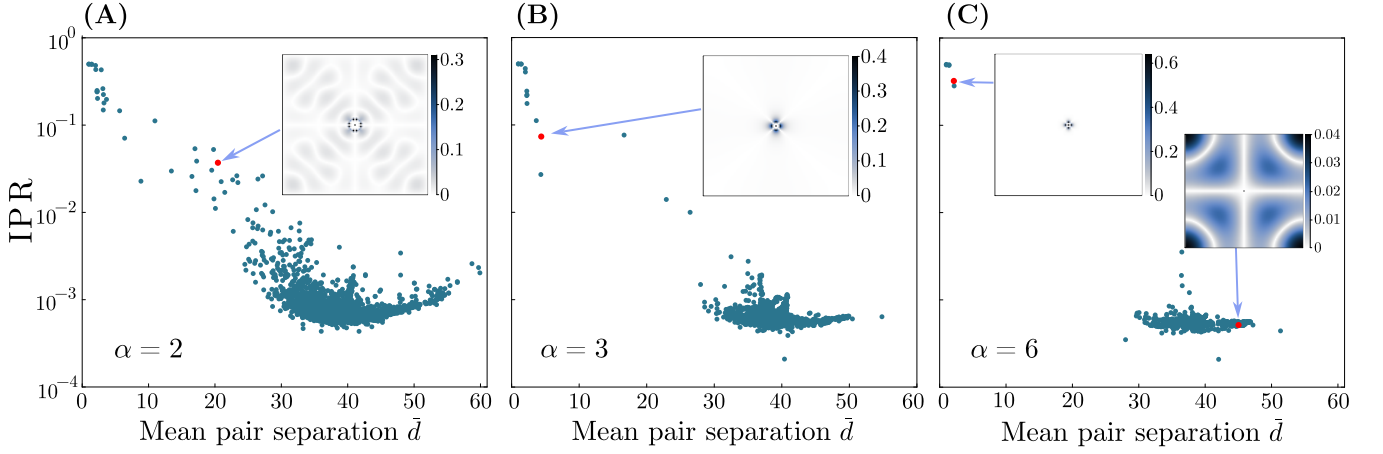


FIG. 3. Eigenstate structure in the two-magnon sector (101×101 , $g/J = 0.2$). Inverse participation ratio (IPR) versus mean pair separation \bar{d} for all eigenstates. (A) $\alpha = 2$: a continuous tail to large \bar{d} indicates bound states and quasilocized states. (B) $\alpha = 3$: intermediate regime with bound states at intermediate separations. (C) $\alpha = 6$: sharp drop in IPR with \bar{d} signals short-range binding only. Insets: real-space distributions of representative eigenstates in the $(\mathbf{r}_1 - \mathbf{r}_2)$ plane.

hibiting persistent oscillations at the same time. Extending the dynamics to times up to $Jt = 60$ for a 9×9 lattice [Fig. 2(A)] reveals that the oscillations in both the longitudinal magnetization $\langle \hat{S}_i^z(t) \rangle$ and the correlation $\tilde{C}(d, t)$ are unconventionally long-lived. To resolve their characteristic frequencies, we perform a discrete Fourier transform \mathcal{F} of $C(d, t)$ and $\langle \hat{S}_i^z(t) \rangle$, applying a Hamming window over the interval $Jt = 5$ – 60 . The resulting spectra exhibit sharp peaks [Fig. 2(B)], signaling the emergence of well-defined modes. To identify their microscopic origin and account for the slow dynamics, we next develop an effective low-energy theory.

Effective few-body theory.—We begin by identifying the low-energy excitations of the unperturbed Hamiltonian $H_0 = -\frac{J}{N_\alpha} \sum_{i \neq j} \frac{\hat{S}_i^z \hat{S}_j^z}{r_{ij}^\alpha}$, with fully polarized initial state $|\downarrow \downarrow \cdots \downarrow\rangle$ as one of the two lowest energy states. Excitations above this background can be described in terms of magnons (or spin flips). For a configuration containing ν magnons at lattice sites $\{i_1, \dots, i_\nu\}$, the energy relative to the ground state energy E_0 is

$$E_\nu(\{i_m\}) - E_0 = 2\nu J \left(1 - \frac{1}{L^2}\right) - \frac{2J}{N_\alpha} \sum_{1 \leq k < l \leq \nu} \frac{1}{r_{i_k i_l}^\alpha}.$$

The first term, which grows linearly with the number of magnons, represents the cost of an isolated magnon. The second term reflects an attractive interaction energy between all magnon pairs.

In the nearest-neighbor limit ($\alpha = \infty$), the interaction term vanishes unless $r_{i_k i_l} = 1$. The energy expression then reduces to a constant proportional to the number of domain-wall links, implying that the excitation spectrum is classified solely by the interface length of spin-flip domains. For finite α , however, the long-range couplings generate a much richer structure. Specifically,

the single-magnon sector forms the lowest excited band, followed by the two-magnon manifold. Higher sectors contain states with three or more magnons, but their ordering is highly sensitive to the geometry of how the magnons are arranged. For example, a compact four-magnon cluster lies energetically below a configuration of three well-separated magnons. Within this hierarchy, the states directly above the two-magnon manifold are those three-magnon configurations in which at least two magnons occupy nearest-neighbor sites.

Having established the structure of low-energy excitations in the pure Ising Hamiltonian, we now focus on the influence of the perturbation $V = -g \sum_i \hat{S}_i^x$. Since, for finite α , the $\nu = 0, 1, 2$ sectors together with the three-magnon sector containing at least a nearest-neighbor pair constitute well-separated excitation bands with gaps of $\mathcal{O}(J)$, the effect of a weak transverse field strength g can be treated perturbatively. Applying a Schrieffer–Wolff (SWT) transformation up to second order in g in each sector, we integrate out couplings to other sectors at leading order and thereby obtain an effective Hamiltonian acting solely within the sector with corrections to this structure arising only at order $\mathcal{O}(g^3/J^2)$. For the two-magnon manifold, imposing translational symmetry and restricting to the zero-momentum subspace, where both the initial state and the dynamics reside, yields the effective Hamiltonian

$$\hat{H}_{\text{eff}}^{(2)} = E_2 + \sum_{\mathbf{d}} U(\mathbf{d}) |\mathbf{d}\rangle \langle \mathbf{d}| + \sum_{\mathbf{d} \neq \mathbf{d}'} t_{\mathbf{d}, \mathbf{d}'} |\mathbf{d}'\rangle \langle \mathbf{d}|. \quad (3)$$

where the basis states $|\mathbf{d}\rangle$ represent two magnons separated by the relative coordinate \mathbf{d} . $E_2 \approx E_0 + 4J - g^2 L^2 / 8J$ fixes the overall energy of the two-magnon manifold. A central finding of our effective description is that two magnons experience an attractive interaction poten-

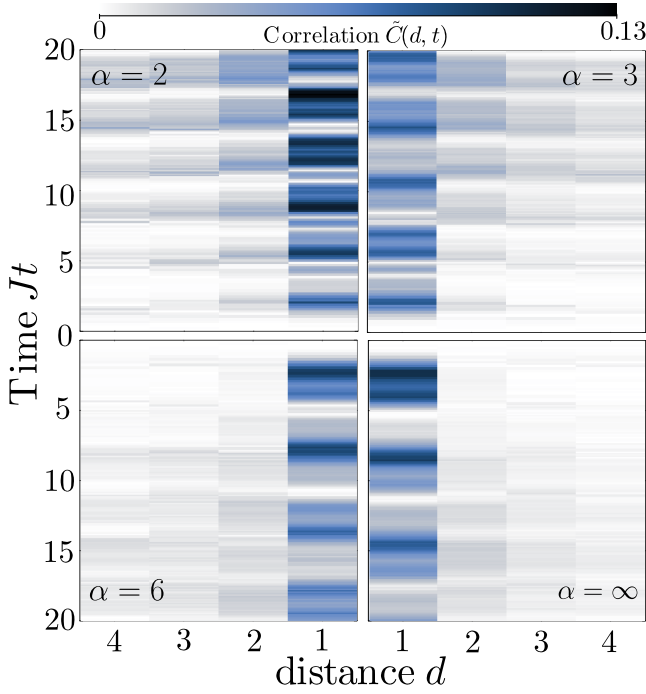


FIG. 4. $\tilde{C}(d, t)$ for a 9×9 lattice with $g/J = 0.2$. The panels compare interaction exponents $\alpha = 2, 3$ with $\alpha = 6$ and the nearest-neighbor limit $\alpha = \infty$.

tial of long-range character,

$$U(\mathbf{d}) = -\left(2J - \frac{g^2}{2J}\right) \frac{1}{\mathcal{N}_\alpha |\mathbf{d}|^\alpha} + \delta U(\mathbf{d}), \quad (4)$$

with $\delta U(\mathbf{d})$ denoting corrections proportional to g^2/J , which at large distances $|\mathbf{d}|$ provide only a subleading contribution to the attractive interactions proportional to $\frac{-g^2}{8J\mathcal{N}_\alpha} \frac{1}{|\mathbf{d}|^{2(\alpha-1)}}$, as long as $\alpha > 2$. The off-diagonal amplitudes $t_{\mathbf{d}, \mathbf{d}'}$ are real and symmetric, describing correlated long-range pair hoppings, which at large $|\mathbf{d} - \mathbf{d}'|$ are given by $t_{\mathbf{d}, \mathbf{d}'} \approx \frac{-g^2}{8J\mathcal{N}_\alpha} \frac{1}{|\mathbf{d} - \mathbf{d}'|^\alpha}$ (explicit derivations are provided in the supplementary material). For all numerical calculations, however, we employ the full (non-asymptotic) effective Hamiltonian derived via the Schrieffer–Wolff transformation. Notice that while an attractive interaction potential might be naturally associated with the formation of bound states in the case of short-range kinetics [31, 32], we find that the interplay between the long-range attractive potential and the correlated pair long-range hoppings produces a rich spectrum of two-magnon bound states.

To validate this theoretical framework, we diagonalize $\hat{H}_{\text{eff}}^{(\nu)}$, and then compare the resulting level spacings with peak positions extracted from the Fourier spectra of $\langle \hat{S}_i^z(t) \rangle$ and $C(d, t)$. Figure 2(B) shows these spectra for 9×9 lattice with $g/J = 0.5$ and $\alpha = 3$ overlaid with excitation gaps $\Delta_{i,j}^{(\nu \leftrightarrow \nu')} = |E_i^\nu - E_j^{\nu'}|$, where E_i^ν denotes the i -th energy level of $\hat{H}_{\text{eff}}^{(\nu)}$. The dominant peak

at $\omega/J \simeq 1.89$ corresponds to $\Delta_{1,1}^{(0 \leftrightarrow 1)}$, i.e., creating a single magnon above the polarized background (see Supplementary Material for the single-magnon dispersion). Additional peaks arise from $\Delta^{(0 \leftrightarrow 2)}$ and $\Delta^{(1 \leftrightarrow 2)}$, corresponding to creating a two-magnon bound state out of the polarized state or out of the single-magnon sector, respectively. We further resolve a peak associated with a three-magnon process $\Delta^{(1 \leftrightarrow 3)}$, corresponding to the creation of three tightly bound magnons. Some peaks appear slightly offset from the exact gap values due to the limited frequency resolution imposed by the NQS time window. As a result, the discrete frequency grid does not include points exactly at those gaps, so the spectral weight appears at the nearest available frequency bin, leading to a small apparent mismatch.

To achieve a more refined frequency resolution, the inset displays the FFT of the exact dynamics for a 5×5 system evolved up to $Jt = 200$. The resulting spectrum agrees very well with the effective predictions, except for the red line. This deviation arises because, for $L \leq 5$, the excitations above the two-magnon manifold, those involving three or more magnons do not form a well-separated band, which limits the applicability of the SWT description. Nevertheless, exact diagonalization reveals that this peak originates from a compact four-magnon cluster. These observations show that the slow dynamics are controlled by a sparse set of well-defined few-magnon excitations rather than a broad many-body continuum. Furthermore, the clear one-to-one correspondence between the spectral peaks extracted from the NQS dynamics and the energy gaps of the effective theory confirms the accuracy of both approaches up to at least $g/J = 0.5$.

Emergence of magnon bound states.—Having validated the few-body theory with our exact numerical simulations with NQS, we now aim to analyze in more detail the two-magnon eigenstates. In this section, we address three central questions: (i) how the spatial structure of the bound states depends on the interaction exponent α , (ii) whether the long-range attractive potential favors bound states beyond the nearest-neighbor separation, and (iii) how these bound states influence the dynamics. In the NN case ($\alpha = \infty$), only nearest-neighbor bound pairs exist, with all other two-magnon configurations forming a broad scattering continuum [33, 34]. Long-range interactions qualitatively change this picture: the attractive potential extends over many lattice spacings, potentially stabilizing bound states at separations far beyond nearest neighbors.

To characterize these states, we analyze the eigenstates $|\psi(\mathbf{d})\rangle$ of the effective two-magnon Hamiltonian $\hat{H}_{\text{eff}}^{(2)}$. For each eigenstate, we compute its inverse participation ratio (IPR), $\text{IPR}[\psi] = \sum_{\mathbf{d}} |\psi(\mathbf{d})|^4$, which distinguishes localized bound pairs (high IPR) from delocalized scattering states (low IPR). Intermediate IPR values correspond to quasilocated states, whose wavefunctions contain a localized core accompanied by a weak delocal-

ized tail. We also compute the mean pair separation, $\bar{d} = \sum_{\mathbf{d}} |\psi(\mathbf{d})|^2 |\mathbf{d}|$, to determine the average relative positions. Figure 3 shows the resulting IPR- \bar{d} distribution for several power-law exponents α on a 101×101 lattice with $g/J = 0.2$, together with representative real-space probability densities in the relative coordinate $(\mathbf{r}_1 - \mathbf{r}_2)$.

For strongly long-ranged interactions ($\alpha = 2$), many eigenstates exhibit a large IPR for mean separations up to $\bar{d} = 4$, followed by a continuous decay of IPR with increasing \bar{d} [Fig. 3(A)]. This indicates that the spectrum contains bound magnon pairs with separations as large as $d = 4$. Furthermore, a substantial fraction of eigenstates displays quasilocalized character, with intermediate values of both IPR and \bar{d} , with a localized component that persists out to separations of $d = 6$. For $\alpha = 3$, the number of quasilocalized states is noticeably reduced [Fig. 3(B)], although bound pairs still survive up to $\bar{d} \approx 4$. These findings demonstrate that long-range interactions stabilize magnons at distances well beyond nearest neighbors and also enhance the number of localized and quasilocalized states. By contrast, in the short-range regime ($\alpha = 6$), only a small number of eigenstates exhibit high IPR, while the majority show low IPR at large \bar{d} . Consequently, the magnon binding is restricted to short separations up to $d \approx \sqrt{2}$ [Fig. 3(C)].

Notice that within the approximation, the effective interaction $U(\mathbf{d})$ in Eq. 4 becomes less attractive as g increases, which correspondingly suppresses the formation of bound states at larger separations. For example, at $g/J = 0.5$ we find that for $\alpha = 2$ and $\alpha = 3$, localized states persist up to separations $d = 2$ and $d = \sqrt{2}$, respectively. For $\alpha = 6$ and $\alpha = \infty$, only nearest-neighbor bound states remain.

Figure 4 shows the time evolution of the correlations $\tilde{C}(d, t)$ for various interaction exponents α at $g/J = 0.2$. A clear distinction emerges between the short-range regime ($\alpha = 6, \infty$) and the long-range regime ($\alpha = 2, 3$). For large α , the signal is stronger at the nearest-neighbor distance $d = 1$, and beyond this separation, the dynamics becomes nearly monochromatic, consistent with the presence of only tight bound magnon pairs and a few characteristic oscillation frequencies. In contrast, for small α , the correlator exhibits multiple frequency components and a significant signal at $d > 1$, reflecting the existence of several extended bound states.

Discussion and Outlook. We study the dynamics of the 2D long-range transverse-field Ising model using large-scale neural quantum state simulations, accessing system sizes and evolution times beyond exact methods. We observe slow relaxation with persistent oscillations after a global quench from a ferromagnetically ordered state. We show that these dynamics are governed by a set of two-magnon bound states stabilized by the long-range attractive interaction. Future experiments with Rydberg arrays and trapped ions could directly probe these spatially extended bound magnons via site-resolved correla-

tion spectroscopy, providing a real-time visualization of bound-pair formation and decay.

Beyond the specific transverse-field Ising dynamics considered here, our framework applies more broadly to long-range interacting systems with different types of kinetic terms—whether generated by bosonic hopping or exchange interactions. The essential ingredient responsible for the emergence of multi-magnon bound states is the long-range attractive potential. Our effective theory reveals that the spin-flip kinetic term renormalizes into a long-range hopping process. Notably, bound states remain stable despite this long-range kinetic motion. Thus we expect that such extended bound states are a generic and robust characteristic of 2D long-range quantum matter.

Data availability.—Data to reproduce all figures are available at Zenodo [35].

Acknowledgements.—The NQS dynamics is simulated using the jVMC package [36], and the exact dynamics are performed with the QuSpin package [37]. This project has received funding from the European Research Council (ERC) under the European Union’s Horizon 2020 research and innovation programme (Grant Agreement No. 853443). This work was supported by the German Research Foundation (DFG) via project 492547816 (TRR 360). We gratefully acknowledge the scientific support and high-performance computing resources provided by the LiCCA HPC cluster at the University of Augsburg and by the Erlangen National High Performance Computing Center (NHR) of the Friedrich-Alexander-Universität Erlangen-Nürnberg (NHR Project No. nqsQuMat). The LiCCA cluster is co-funded by the DFG (Project ID 499211671). NHR funding is provided by federal and Bavarian state authorities, and the NHR@FAU hardware is partially funded by the DFG (Grant No. 440719683).

Note added.—During the preparation of this manuscript, we became aware of related work by Kaltenmark *et al.* [38], who study spectroscopic signatures in a kinetically constrained long-range interacting two-dimensional spin system. While their microscopic model and parameter regime differ from ours, both works highlight the emergence of nontrivial elementary excitations in long-range interacting quantum systems.

-
- [1] N. Defenu, T. Donner, T. Macrì, G. Pagano, S. Ruffo, and A. Trombettoni, Long-range interacting quantum systems, *Rev. Mod. Phys.* **95**, 035002 (2023).
 - [2] J. W. Britton, B. C. Sawyer, A. C. Keith, C.-C. J. Wang, J. K. Freericks, H. Uys, M. J. Biercuk, and J. J. Bollinger, Engineered two-dimensional ising interactions in a trapped-ion quantum simulator with hundreds of spins, *Nature* **484**, 489 (2012).
 - [3] P. Richerme, Z.-X. Gong, A. Lee, C. Senko, J. Smith,

- M. Foss-Feig, S. Michalakis, A. V. Gorshkov, and C. Monroe, Non-local propagation of correlations in quantum systems with long-range interactions, *Nature* **511**, 198 (2014).
- [4] P. Jurcevic, B. P. Lanyon, P. Hauke, C. Hempel, P. Zoller, R. Blatt, and C. F. Roos, Quasiparticle engineering and entanglement propagation in a quantum many-body system, *Nature* **511**, 202 (2014).
- [5] J. G. Bohnet, B. C. Sawyer, J. W. Britton, M. L. Wall, A. M. Rey, M. Foss-Feig, and J. J. Bollinger, Quantum spin dynamics and entanglement generation with hundreds of trapped ions, *Science* **352**, 1297 (2016).
- [6] J. Zhang, G. Pagano, P. W. Hess, A. Kyprianidis, P. Becker, H. Kaplan, A. V. Gorshkov, Z.-X. Gong, and C. Monroe, Observation of a many-body dynamical phase transition with a 53-qubit quantum simulator, *Nature* **551**, 601 (2017).
- [7] C. Monroe, W. C. Campbell, L.-M. Duan, Z.-X. Gong, A. V. Gorshkov, P. W. Hess, R. Islam, K. Kim, N. M. Linke, G. Pagano, P. Richerme, C. Senko, and N. Y. Yao, Programmable quantum simulations of spin systems with trapped ions, *Rev. Mod. Phys.* **93**, 025001 (2021).
- [8] K. Kim, F. Yang, K. Mølmer, and J. Ahn, Realization of an extremely anisotropic heisenberg magnet in rydberg atom arrays, *Phys. Rev. X* **14**, 011025 (2024).
- [9] A. Browaeys and T. Lahaye, Many-body physics with individually controlled rydberg atoms, *Nature Physics* **16**, 132 (2020).
- [10] S. Ebadi, T. T. Wang, H. Levine, A. Keesling, G. Semeghini, A. Omran, D. Bluvstein, R. Samajdar, H. Pichler, W. W. Ho, *et al.*, Quantum phases of matter on a 256-atom programmable quantum simulator, *Nature* **595**, 227 (2021).
- [11] G. Bornet, G. Emperauger, C. Chen, B. Ye, M. Block, M. Bintz, J. A. Boyd, D. Barredo, T. Comparin, F. Mez-zacapo, *et al.*, Scalable spin squeezing in a dipolar rydberg atom array, *Nature* **621**, 728 (2023).
- [12] B. Yan, S. A. Moses, B. Gadway, J. P. Covey, K. R. Hazzard, A. M. Rey, D. S. Jin, and J. Ye, Observation of dipolar spin-exchange interactions with lattice-confined polar molecules, *Nature* **501**, 521 (2013).
- [13] K. R. A. Hazzard, B. Gadway, M. Foss-Feig, B. Yan, S. A. Moses, J. P. Covey, N. Y. Yao, M. D. Lukin, J. Ye, D. S. Jin, and A. M. Rey, Many-body dynamics of dipolar molecules in an optical lattice, *Phys. Rev. Lett.* **113**, 195302 (2014).
- [14] L. Christakis, J. S. Rosenberg, R. Raj, S. Chi, A. Morningstar, D. A. Huse, Z. Z. Yan, and W. S. Bakr, Probing site-resolved correlations in a spin system of ultracold molecules, *Nature* **614**, 64 (2023).
- [15] A. de Paz, A. Sharma, A. Chotia, E. Maréchal, J. H. Huckans, P. Pedri, L. Santos, O. Gorceix, L. Vernac, and B. Laburthe-Tolra, Nonequilibrium quantum magnetism in a dipolar lattice gas, *Phys. Rev. Lett.* **111**, 185305 (2013).
- [16] Y. A. Alaoui, B. Zhu, S. R. Muleady, W. Dubosclard, T. Roscilde, A. M. Rey, B. Laburthe-Tolra, and L. Vernac, Measuring correlations from the collective spin fluctuations of a large ensemble of lattice-trapped dipolar spin-3 atoms, *Phys. Rev. Lett.* **129**, 023401 (2022).
- [17] P. Hauke and L. Tagliacozzo, Spread of correlations in long-range interacting quantum systems, *Phys. Rev. Lett.* **111**, 207202 (2013).
- [18] F. Liu, R. Lundgren, P. Titum, G. Pagano, J. Zhang, C. Monroe, and A. V. Gorshkov, Confined quasiparticle dynamics in long-range interacting quantum spin chains, *Phys. Rev. Lett.* **122**, 150601 (2019).
- [19] H. Bethe, Zur theorie der metalle, *Zeitschrift für Physik* **71**, 205 (1931).
- [20] M. Wortis, Bound states of two spin waves in the heisenberg ferromagnet, *Phys. Rev.* **132**, 85 (1963).
- [21] F. Kranzl, S. Birnkammer, M. K. Joshi, A. Bastianello, R. Blatt, M. Knap, and C. F. Roos, Observation of magnon bound states in the long-range, anisotropic heisenberg model, *Phys. Rev. X* **13**, 031017 (2023).
- [22] T. Fukuhara, P. Schauß, M. Endres, S. Hild, M. Cheneau, I. Bloch, and C. Gross, Microscopic observation of magnon bound states and their dynamics, *Nature* **502**, 76 (2013).
- [23] T. Macrì, L. Lepori, G. Pagano, M. Lewenstein, and L. Barbiero, Bound state dynamics in the long-range spin- $\frac{1}{2}$ xxz model, *Phys. Rev. B* **104**, 214309 (2021).
- [24] G. Carleo and M. Troyer, Solving the quantum many-body problem with artificial neural networks, *Science* **355**, 602 (2017).
- [25] M. Schmitt and M. Heyl, Quantum many-body dynamics in two dimensions with artificial neural networks, *Phys. Rev. Lett.* **125**, 100503 (2020).
- [26] M. Schmitt, M. M. Rams, J. Dziarmaga, M. Heyl, and W. H. Zurek, Quantum phase transition dynamics in the two-dimensional transverse-field ising model, *Science Advances* **8**, eabl6850 (2022).
- [27] M. Schmitt and M. Heyl, Simulating dynamics of correlated matter with neural quantum states (2025), [arXiv:2506.03124 \[quant-ph\]](https://arxiv.org/abs/2506.03124).
- [28] K. He, X. Zhang, S. Ren, and J. Sun, Deep residual learning for image recognition (2015), [arXiv:1512.03385 \[cs.CV\]](https://arxiv.org/abs/1512.03385).
- [29] A. Chen and M. Heyl, Empowering deep neural quantum states through efficient optimization, *Nature Physics* **20**, 1476 (2024).
- [30] A. Chen, V. D. Naik, and M. Heyl, Convolutional transformer wave functions (2025), [arXiv:2503.10462 \[cond-mat.dis-nn\]](https://arxiv.org/abs/2503.10462).
- [31] K. Yang and M. de Llano, Simple variational proof that any two-dimensional potential well supports at least one bound state, *American Journal of Physics* **57**, 85 (1989).
- [32] K. Chadán, N. Khuri, A. Martin, and T. Tsun Wu, Bound states in one and two spatial dimensions, *Journal of Mathematical Physics* **44**, 406 (2003).
- [33] J. Tindall and D. Sels, Confinement in the transverse field ising model on the heavy hex lattice, *Phys. Rev. Lett.* **133**, 180402 (2024).
- [34] L. Pavešić, D. Jaschke, and S. Montangero, Constrained dynamics and confinement in the two-dimensional quantum ising model, *Phys. Rev. B* **111**, L140305 (2025).
- [35] V. D. Naik and M. Heyl, Slow dynamics and magnon bound states in the 2d long-range quantum ising model (2025).
- [36] M. Schmitt and M. Reh, jVMC: Versatile and performant variational Monte Carlo leveraging automated differentiation and GPU acceleration, *SciPost Phys. Codebases* , 2 (2022).
- [37] P. Weinberg and M. Bukov, QuSpin: a Python package for dynamics and exact diagonalisation of quantum many body systems part I: spin chains, *SciPost Phys.* **2**, 003 (2017).
- [38] T. Kaltenmark, C. Nill, C. Groß, and I. Lesanovsky,

End Matter

Appendix A: Neural quantum state simulations.—We represent the many-body wavefunction by a neural quantum state (NQS) $\psi_{\boldsymbol{\theta}}(S, t)$, where $S \in \{\pm 1\}^{L \times L}$ and $\boldsymbol{\theta}$ are trainable parameters. Real-time dynamics follows the time-dependent variational principle (TDVP), which projects the Schrödinger equation onto the NQS manifold:

$$\sum_b S_{ab} \dot{\theta}_b = -i F_a, \quad (\text{A1})$$

$$S_{ab} = \langle O_a^\dagger O_b \rangle_c, \quad F_a = \langle O_a^\dagger E_{\text{loc}} \rangle_c, \quad (\text{A2})$$

with logarithmic derivatives $O_a(S, t) = \partial_{\theta_a} \ln \psi_{\boldsymbol{\theta}}(S, t)$, connected correlators $\langle \cdot \rangle_c$ over $|\psi_{\boldsymbol{\theta}}|^2$, and local energy $E_{\text{loc}}(S) = \sum_{S'} H_{SS'} \psi_{\boldsymbol{\theta}}(S') / \psi_{\boldsymbol{\theta}}(S)$. We integrate the equation of motion $S \dot{\boldsymbol{\theta}} = -i \mathbf{F}$ using a Heun solver, which provides a second-order update for $\boldsymbol{\theta}(t)$.

We employ a convolutional neural network (CNN) based on the ResNet framework, with Gaussian Error Linear Unit (GELU) activation functions. We enforce lattice translation invariance by using the convolutions with periodic padding. The convolutional blocks produce a final set of real-valued feature maps. These maps are then split to generate the real and imaginary parts of an intermediate complex feature map. A global logsum-exp pooling operation is applied across all spatial positions and feature channels of this map to produce a base scalar log-wavefunction. To produce the final NQS, we additionally impose the point-group symmetries of the square lattice (rotations and reflections), by averaging the exponentiated base wavefunction over all symmetric operations at the output layer. We use networks consisting of two ResNet blocks with 3×3 filter kernels and 16 feature channels for all simulations presented in this work.

All simulations are performed in the \hat{S}^z basis, where each configuration S in $\psi_{\boldsymbol{\theta}}(S)$ denotes a spin configuration along the z -direction. Although the Hamiltonian 1 is written in the $ZZ + X$ form in the main text, we implement the NQS simulations using the equivalent rotated $XX + Z$ representation. This choice ensures that the ferromagnetically ordered initial state corresponds to a uniformly distributed wavefunction in the configuration space, rather than a single delta peak, which removes instabilities coming from zeroes of the wavefunction.

Expectation values in Eq. (A2) are estimated using Markov-chain Monte Carlo sampling with Metropolis single-spin-flip updates. For each time step, we use $5 \times L^2$ sweeps for thermal equilibration, followed by

$3 \times 10^4 - 4 \times 10^4$ measurement sweeps. We use an adaptive Heun scheme for the integration of the TDVP equation, with integration tolerance of 10^{-4} .

Appendix B: Spectral analysis.—To extract excitation energies, we compute the discrete Fourier transform (FFT) of $\mathcal{O}(t) \in \{C(d, t), \langle \hat{S}_i^z(t) \rangle\}$ over a finite time and apply a Hamming window to reduce spectral leakage. With $t_n = n \Delta t$ and $n = 0, \dots, N_t - 1$, we define $w_n = 0.54 - 0.46 \cos\left(\frac{2\pi n}{N_t - 1}\right)$, and the transform

$$\mathcal{F}(\mathcal{O}(t))(\omega_k) = \sum_{n=0}^{N_t-1} w_n [\mathcal{O}(t_n) - \bar{\mathcal{O}}] e^{i\omega_k t_n}, \quad (\text{A3})$$

where $\bar{\mathcal{O}} = \frac{1}{N_t} \sum_{n=0}^{N_t-1} \mathcal{O}(t_n)$ removes the zero-frequency component and $\omega_k = \frac{2\pi k}{N_t \Delta t}$ with $k = 0, \dots, N_t - 1$. Peaks in $|\mathcal{F}(\mathcal{O}(t))(\omega_k)|$ identify the frequencies governing the dynamics. These peak positions are compared to energy differences $|E_i^\nu - E_j^{\nu'}|$ obtained by diagonalizing the effective few-magnon Hamiltonians $\hat{H}_{\text{eff}}^{(\nu)}$, allowing us to assign each spectral line to a single-magnon or a multi-magnon bound state.

Supplemental Material: Slow dynamics and magnon bound states in the 2D long-range quantum Ising model

Schrieffer–Wolff transformation.

This section derives the effective few-magnon Hamiltonian using the Schrieffer–Wolff (SW) transformation. A configuration with ν magnons at positions i_1, \dots, i_ν has unperturbed energy

$$E_\nu(\{i_m\}) = E_0 + 2\nu J \left(1 - \frac{1}{L^2}\right) - \frac{2J}{\mathcal{N}_\alpha} \sum_{1 \leq k < l \leq \nu} \frac{1}{r_{i_k i_l}^\alpha}.$$

where $E_0 = -(L^2 - 1)/2$ denotes the energy of the fully polarized state and only energy differences enter the SW expansion. With zero magnon states being the lowest energy band, $E_\nu(\{i_m\})$ helps to determine the structure of low-energy excitations. In the nearest-neighbor limit ($\alpha = \infty$), the energy levels are classified solely by the interface length. For finite α , zero-, one-, and two-magnon sectors form well-separated excitation bands with gaps of order $\mathcal{O}(J)$.

Introducing a weak transverse field $g\hat{T} = -\sum_i \hat{S}_i^x$, couples different ν sectors only perturbatively. To eliminate these couplings at leading order, we perform the Schrieffer–Wolff (SW) transformation $\hat{H}_{\text{SW}} = e^{\hat{S}} \hat{H} e^{-\hat{S}}$, and choose the generator \hat{S} such that $[\hat{S}, \hat{H}_0] = -g\hat{T}$, which removes matrix elements between the ν and $\nu \pm 1$ sectors to first order in g . Projecting onto the ν -magnon manifold \mathcal{P}_ν gives

$$\hat{H}_{\text{eff}}^{(\nu)} = P_\nu \hat{H}_0 P_\nu + \frac{g^2}{2} P_\nu [\hat{S}, \hat{T}] P_\nu + \mathcal{O}(g^3/J^2).$$

Using the standard expression for \hat{S} in terms of virtual transitions, we obtain

$$\hat{H}_{\text{eff}}^{(\nu)} = \sum_m E_\nu(m) |m\rangle\langle m| + \frac{g^2}{2} \sum_{m,n,\beta} \langle m|\hat{T}|\beta\rangle \langle \beta|\hat{T}|n\rangle \left(\frac{1}{E_m - E_\beta} + \frac{1}{E_n - E_\beta} \right) |m\rangle\langle n|,$$

where $\{|m\rangle\}$ spans the ν -magnon space \mathcal{P}_ν , and $|\beta\rangle$ runs over virtual states in the complement $\mathcal{Q}_\nu = 1 - \mathcal{P}_\nu$ (i.e., the $\nu - 1$ and $\nu + 1$ sectors). This equation provides the leading $\mathcal{O}(g^2/J)$ corrections that define the effective few-magnon Hamiltonian used in the main text.

Effective zero-magnon Hamiltonian

In the zero-magnon sector ($\nu = 0$) there is only a single basis state. The effective Hamiltonian $\hat{H}_{\text{eff}}^{(0)}$ therefore reduces to the diagonal energy

$$E_{\text{eff}}^{(0)} = E_0 + g^2 \sum_\beta \frac{|\langle 0|\hat{T}|\beta\rangle|^2}{E_0 - E_\beta},$$

where $|\beta\rangle$ runs over all single-magnon states, and all single-magnon states lie at energy $E_\beta = E_0 + 2J(1 - \frac{1}{L^2})$. Summing over the L^2 possible single-flip configurations gives

$$E_{\text{eff}}^{(0)} = E_0 - \frac{g^2}{8J} \frac{L^2}{(1 - 1/L^2)} \approx E_0 - \frac{g^2 L^2}{8J}.$$

Effective single-magnon Hamiltonian.

In the single-magnon sector ($\nu = 1$), the effective Hamiltonian $\hat{H}_{\text{eff}}^{(1)}$ can be written as

$$\hat{H}_{\text{eff}}^{(1)} = E_1 \sum_i |i\rangle\langle i| + g^2 \sum_{i,j,\beta} \frac{\langle i|\hat{T}|\beta\rangle \langle \beta|\hat{T}|j\rangle}{E_1 - E_\beta} |i\rangle\langle j|, \quad (\text{S1})$$

where $|i\rangle$ are single-flip states with i denoting the position of the magnon, and $E_1 = E_0 + 2J(1 - \frac{1}{L^2})$. Here $|\beta\rangle$ is either the zero-magnon state or any of the two-magnon states.

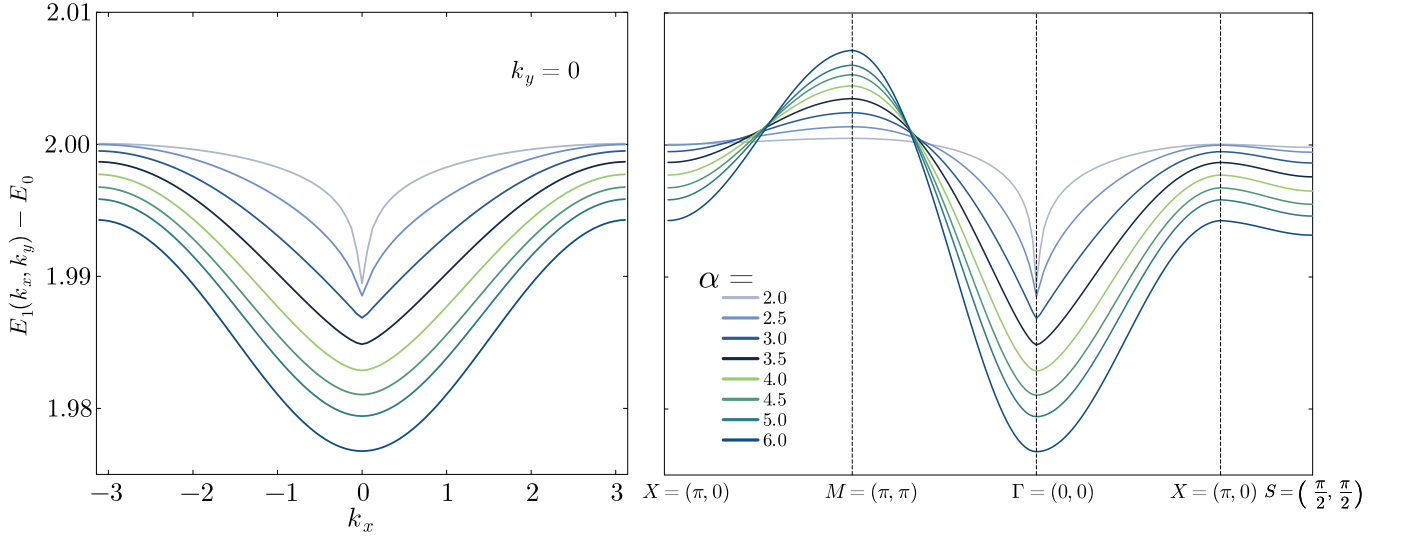


FIG. S1. Single-magnon dispersion for different power-law exponents α . Left: dispersion $E_1(k_x, k_y=0) - E_0$ along the k_x direction. Right: dispersion along the high-symmetry path $X \rightarrow M \rightarrow \Gamma \rightarrow X \rightarrow S$. Long-range interactions induce a nonanalytic cusp at Γ , which gradually disappears as α becomes large.

Diagonal term. The diagonal term also acquires a second-order correction in g to E_1 ,

$$\begin{aligned} U_i &= E_0 + 2J \left(1 - \frac{1}{L^2}\right) + g^2 \sum_{\beta \in (0,2)\text{-flip}} \frac{|\langle i | \hat{T} | \beta \rangle|^2}{E_1 - E_\beta} \\ &= E_0 + 2J \left(1 - \frac{1}{L^2}\right) + \frac{g^2}{8J \left(1 - \frac{1}{L^2}\right)} - \frac{g^2}{4} \sum_{j \neq i} \frac{1}{2J \left(1 - \frac{1}{L^2}\right) - \frac{2J}{\mathcal{N}_\alpha |r_{ij}|^\alpha}}. \end{aligned}$$

Taking the large- L limit, and writing $\mathbf{d} = r_{ij}$, this simplifies to

$$U \approx E_0 + 2J + \frac{g^2}{8J} - \frac{g^2}{8J} \sum_{|\mathbf{d}| \neq 0} \left(1 - \frac{1}{\mathcal{N}_\alpha |\mathbf{d}|^\alpha}\right)^{-1}.$$

Expanding $\left(1 - \frac{1}{\mathcal{N}_\alpha |\mathbf{d}|^\alpha}\right)^{-1}$ to first order in $\frac{1}{|\mathbf{d}|^\alpha}$, we obtain

$$\begin{aligned} U &\approx E_0 + 2J + \frac{g^2}{8J} - \frac{g^2}{8J} \sum_{|\mathbf{d}| \neq 0} \left(1 + \frac{1}{\mathcal{N}_\alpha |\mathbf{d}|^\alpha}\right) \\ &= E_0 + 2J + \frac{g^2}{8J} - \frac{g^2(L^2 - 1)}{8J} - \frac{g^2}{8J\mathcal{N}_\alpha} \sum_{|\mathbf{d}| \neq 0} \frac{1}{|\mathbf{d}|^\alpha} \\ &= E_0 + 2J - \frac{g^2 L^2}{8J}. \end{aligned}$$

Therefore, in the large- L limit the diagonal part of $\hat{H}_{\text{eff}}^{(1)}$ is well approximated by

$$U \approx E_0 + 2J - \frac{g^2 L^2}{8J}.$$

Off-diagonal term. The off-diagonal matrix elements between two single-magnon states are given by

$$\begin{aligned} t_{i,j} &= g^2 \sum_{\beta \in (0,2)\text{-flip}} \frac{\langle i | \hat{T} | \beta \rangle \langle \beta | \hat{T} | j \rangle}{E_1 - E_\beta} \\ &= \frac{g^2}{4} \left(\frac{1}{2J \left(1 - \frac{1}{L^2}\right)} - \frac{1}{2J \left(1 - \frac{1}{L^2}\right) - \frac{2J}{|r_{ij}|^\alpha}} \right). \end{aligned}$$

Taking again the large- L limit and expanding to first order in $\frac{1}{|r_{ij}|^\alpha}$, we obtain

$$t_{i,j} \approx -\frac{g^2}{8J\mathcal{N}_\alpha} \left(\frac{1}{|r_{ij}|^\alpha - 1/\mathcal{N}_\alpha} \right) \approx -\frac{g^2}{8J\mathcal{N}_\alpha} \frac{1}{|r_{ij}|^\alpha}.$$

Combining the diagonal and off-diagonal processes, the effective single-magnon Hamiltonian becomes

$$\hat{H}_{\text{eff}}^{(1)} = \left(E_0 + 2J - \frac{g^2 L^2}{8J} \right) - \frac{g^2}{8J\mathcal{N}_\alpha} \sum_{i \neq j} \frac{1}{|r_{ij}|^\alpha} |i\rangle \langle j|.$$

Figure S1 displays the single-magnon dispersion for different power-law exponents.

Effective two-magnon Hamiltonian.

In the two-magnon sector ($\nu = 2$), the effective Hamiltonian $\hat{H}_{\text{eff}}^{(2)}$ can be written as

$$\begin{aligned} \hat{H}_{\text{eff}}^{(2)} = & \sum_{n_1, n_2} E_2(n_1, n_2) |n_1, n_2\rangle \langle n_1, n_2| + \frac{g^2}{2} \sum_{n_1, n_2, m_1, m_2, \beta} \langle n_1, n_2 | \hat{T} | \beta \rangle \langle \beta | \hat{T} | m_1, m_2 \rangle \\ & \times \left(\frac{1}{E_2(n_1, n_2) - E_\beta} + \frac{1}{E_2(m_1, m_2) - E_\beta} \right) |n_1, n_2\rangle \langle m_1, m_2|. \end{aligned}$$

Here $|n_1, n_2\rangle$ are two-flip states inside the two-magnon subspace \mathcal{P} , while $|\beta\rangle$ are virtual states in the complement $\mathcal{Q} = 1 - \mathcal{P}$ (i.e., the one-flip and three-flip sectors), and

$$E_2(n_1, n_2) = E_0 + 4J \left(1 - \frac{1}{L^2} \right) - \frac{2J}{\mathcal{N}_\alpha} \frac{1}{r_{n_1, n_2}^\alpha}.$$

Diagonal term. We now switch to relative coordinates by pinning one flipped spin and labeling basis states by the displacement $\mathbf{d} = \mathbf{n}_2 - \mathbf{n}_1$, so that $|\mathbf{d}\rangle$ denotes a two-magnon state with separation \mathbf{d} . The diagonal term then acquires a second-order correction in g ,

$$\begin{aligned} U(\mathbf{d}) = & E_0 + 4J \left(1 - \frac{1}{L^2} \right) - \frac{2J}{\mathcal{N}_\alpha} \frac{1}{|\mathbf{d}|^\alpha} + g^2 \sum_{\beta \in (1,3)\text{-flip}} \frac{|\langle \mathbf{d} | \hat{T} | \beta \rangle|^2}{E_2(\mathbf{d}) - E_\beta} \\ = & E_0 + 4J \left(1 - \frac{1}{L^2} \right) - \frac{2J}{\mathcal{N}_\alpha} \frac{1}{|\mathbf{d}|^\alpha} \\ & + \frac{g^2}{4} \left[\frac{2}{2J \left(1 - \frac{1}{L^2} \right) - \frac{2J}{\mathcal{N}_\alpha} \frac{1}{|\mathbf{d}|^\alpha}} - \sum_{\substack{\mathbf{d}' \neq (0,0) \\ \mathbf{d}' \neq \mathbf{d}}} \frac{1}{2J \left(1 - \frac{1}{L^2} \right) - \frac{2J}{\mathcal{N}_\alpha} \left[\frac{1}{|\mathbf{d}'|^\alpha} + \frac{1}{|\mathbf{d} - \mathbf{d}'|^\alpha} \right]} \right]. \end{aligned}$$

Taking the large- L limit gives the leading-order corrections. The first correction term can be written as

$$\frac{g^2}{8J} \frac{2}{\left(1 - \frac{1}{\mathcal{N}_\alpha} \frac{1}{|\mathbf{d}|^\alpha} \right)} = \frac{g^2}{4J} \left[1 - \frac{1}{\mathcal{N}_\alpha} \frac{1}{|\mathbf{d}|^\alpha} \right]^{-1} \approx \frac{g^2}{4J} \left[1 + \frac{1}{\mathcal{N}_\alpha} \frac{1}{|\mathbf{d}|^\alpha} \right] = \frac{g^2}{4J} + \frac{g^2}{4J\mathcal{N}_\alpha} \frac{1}{|\mathbf{d}|^\alpha}.$$

The second correction term is

$$\begin{aligned}
\frac{g^2}{8J} \sum_{\substack{\mathbf{d}' \neq (0,0) \\ \mathbf{d}' \neq \mathbf{d}}} \left[\frac{1}{1 - \frac{1}{\mathcal{N}_\alpha} \left(\frac{1}{|\mathbf{d}'|^\alpha} + \frac{1}{|\mathbf{d} - \mathbf{d}'|^\alpha} \right)} \right] &= \frac{g^2}{8J} \sum_{\substack{\mathbf{d}' \neq (0,0) \\ \mathbf{d}' \neq \mathbf{d}}} \left[1 + \sum_{i=1}^{\infty} \left(\frac{1}{\mathcal{N}_\alpha} \right)^i \left(\frac{1}{|\mathbf{d}'|^\alpha} + \frac{1}{|\mathbf{d} - \mathbf{d}'|^\alpha} \right)^i \right] \\
&= \frac{g^2(L^2 - 2)}{8J} + \frac{g^2}{8J} \sum_{i=1}^{\infty} \left[\left(\frac{1}{\mathcal{N}_\alpha} \right)^i \sum_{\substack{\mathbf{d}' \neq (0,0) \\ \mathbf{d}' \neq \mathbf{d}}} \left(\frac{1}{|\mathbf{d}'|^\alpha} + \frac{1}{|\mathbf{d} - \mathbf{d}'|^\alpha} \right)^i \right] \\
&= \frac{g^2(L^2 - 2)}{8J} + \frac{g^2}{8J} \sum_{i=1}^{\infty} \left[\left(\frac{1}{\mathcal{N}_\alpha} \right)^i \sum_{m=0}^i \binom{i}{m} \sum_{\substack{\mathbf{d}' \neq (0,0) \\ \mathbf{d}' \neq \mathbf{d}}} \frac{1}{|\mathbf{d}'|^{m\alpha} |\mathbf{d} - \mathbf{d}'|^{(i-m)\alpha}} \right].
\end{aligned}$$

Separating the \mathbf{d} -dependent terms, we obtain

$$\begin{aligned}
\frac{g^2}{8J} \sum_{\substack{\mathbf{d}' \neq (0,0) \\ \mathbf{d}' \neq \mathbf{d}}} \left[\frac{1}{1 - \frac{1}{\mathcal{N}_\alpha} \left(\frac{1}{|\mathbf{d}'|^\alpha} + \frac{1}{|\mathbf{d} - \mathbf{d}'|^\alpha} \right)} \right] &= \frac{g^2(L^2 - 2)}{8J} + \frac{g^2}{4J} \sum_{i=1}^{\infty} \left(\frac{1}{\mathcal{N}_\alpha} \right)^i \left(\sum_{\mathbf{d}' \neq (0,0)} \frac{1}{|\mathbf{d}'|^{i\alpha}} \right) \\
&\quad - \frac{g^2}{4J} \sum_{i=1}^{\infty} \left(\frac{1}{\mathcal{N}_\alpha} \right)^i \frac{1}{|\mathbf{d}|^{i\alpha}} + \frac{g^2}{8J} \sum_{i=2}^{\infty} \left(\frac{1}{\mathcal{N}_\alpha} \right)^i \sum_{m=2}^{i-1} \mathcal{F}_m^i(\mathbf{d}),
\end{aligned}$$

where

$$\mathcal{F}_m^i(\mathbf{d}) = \sum_{\substack{\mathbf{d}' \neq (0,0) \\ \mathbf{d}' \neq \mathbf{d}}} \frac{1}{|\mathbf{d}'|^{m\alpha} |\mathbf{d} - \mathbf{d}'|^{(i-m)\alpha}}$$

can be evaluated for large $|\mathbf{d}|$ by approximating the sum by a continuum integral,

$$\mathcal{F}_m^i(R) = \int d^2r \frac{1}{|r|^{m\alpha} |r - R|^{(i-m)\alpha}}.$$

Using the homogeneous function property, one finds

$$\mathcal{F}_m^i(\lambda R) = \frac{1}{\lambda^{(i\alpha-2)}} \mathcal{F}_m^i(R) \quad \Rightarrow \quad \mathcal{F}_m^i(R) = \frac{\mathcal{F}_m^i(1)}{R^{(i\alpha-2)}}.$$

Having all these ingredients, we can now write down the second correction term, ignoring higher-order contributions in i :

$$\frac{g^2(L^2 + 2)}{8J} - \frac{g^2}{4J\mathcal{N}_\alpha} \frac{1}{|\mathbf{d}|^\alpha} + \frac{g^2}{8J\mathcal{N}_\alpha^2} \frac{\mathcal{F}_{m=1}^{i=2}(1)}{|\mathbf{d}|^{2(\alpha-1)}}.$$

Finally, combining everything gives the expression for $U(\mathbf{d})$:

$$\tilde{U}(\mathbf{d}) = E_0 + 4J - \frac{g^2 L^2}{8J} - \frac{(2J - g^2/2J)}{\mathcal{N}_\alpha} \frac{1}{|\mathbf{d}|^\alpha},$$

and we isolate the \mathbf{d} -dependent potential as

$$U(\mathbf{d}) = -\frac{(2J - g^2/2J)}{\mathcal{N}_\alpha} \frac{1}{|\mathbf{d}|^\alpha}.$$

Off-diagonal term. The off-diagonal matrix elements between distinct separations are

$$\begin{aligned}
t_{\mathbf{d},\mathbf{d}'} &= \frac{g^2}{2} \sum_{\beta \in (1,3)\text{-flip}} \langle \mathbf{d} | \hat{T} | \beta \rangle \langle \beta | \hat{T} | \mathbf{d}' \rangle \left(\frac{1}{E_2(\mathbf{d}) - E_\beta} + \frac{1}{E_2(\mathbf{d}') - E_\beta} \right) \\
&= \frac{g^2}{8} \left(\frac{1}{2J(1 - 1/L^2) - \frac{2J}{\mathcal{N}_\alpha} \frac{1}{|\mathbf{d}|^\alpha}} + \frac{1}{2J(1 - 1/L^2) - \frac{2J}{\mathcal{N}_\alpha} \frac{1}{|\mathbf{d}'|^\alpha}} \right) \\
&\quad - \frac{g^2}{8} \left(\frac{1}{2J(1 - 1/L^2) - \frac{2J}{\mathcal{N}_\alpha} \left(\frac{1}{|\mathbf{d}'|^\alpha} + \frac{1}{|\mathbf{d}-\mathbf{d}'|^\alpha} \right)} + \frac{1}{2J(1 - 1/L^2) - \frac{2J}{\mathcal{N}_\alpha} \left(\frac{1}{|\mathbf{d}|^\alpha} + \frac{1}{|\mathbf{d}-\mathbf{d}'|^\alpha} \right)} \right).
\end{aligned}$$

Taking the large- L limit and expanding to first order in $\frac{1}{|\mathbf{d}|^\alpha}$, we get

$$\begin{aligned}
t_{\mathbf{d},\mathbf{d}'} &\approx \frac{g^2}{16J} \left(1 + \frac{1}{\mathcal{N}_\alpha} \frac{1}{|\mathbf{d}|^\alpha} + 1 + \frac{1}{\mathcal{N}_\alpha} \frac{1}{|\mathbf{d}'|^\alpha} \right. \\
&\quad \left. - 1 - \frac{1}{\mathcal{N}_\alpha} \left(\frac{1}{|\mathbf{d}|^\alpha} + \frac{1}{|\mathbf{d}-\mathbf{d}'|^\alpha} \right) - 1 - \frac{1}{\mathcal{N}_\alpha} \left(\frac{1}{|\mathbf{d}'|^\alpha} + \frac{1}{|\mathbf{d}-\mathbf{d}'|^\alpha} \right) \right),
\end{aligned}$$

which simplifies to

$$t_{\mathbf{d},\mathbf{d}'} \approx -\frac{g^2}{8J\mathcal{N}_\alpha} \frac{1}{|\mathbf{d}-\mathbf{d}'|^\alpha}.$$

Combining the diagonal and off-diagonal processes gives

$$\boxed{\hat{H}_{\text{eff}}^{(2)} = E_2 + \sum_{\mathbf{d}} U(\mathbf{d}) |\mathbf{d}\rangle \langle \mathbf{d}| + \sum_{\mathbf{d} \neq \mathbf{d}'} t_{\mathbf{d},\mathbf{d}'} |\mathbf{d}\rangle \langle \mathbf{d}'|},$$

with

$$E_2 \approx E_0 + 4J - \frac{g^2 L^2}{8J}, \quad U(\mathbf{d}) \approx -\frac{(2J - g^2/2J)}{\mathcal{N}_\alpha} \frac{1}{|\mathbf{d}|^\alpha}, \quad t_{\mathbf{d},\mathbf{d}'} \approx -\frac{g^2}{8J\mathcal{N}_\alpha} \frac{1}{|\mathbf{d}-\mathbf{d}'|^\alpha}.$$